Mapping the Distribution of Electron Temperature and Fe Charge States in the Corona with Total Solar Eclipse Observations

Habbal, Shadia Rifai; Druckmüller, M.; Morgan, H.; Daw, A.; Johnson, J.; Ding, A.; Arndt, M.; Esser, R.; Rušin, V.; Scholl, I.

Published in:
Astrophysical Journal

DOI:
10.1088/0004-637X/708/2/1650

Publication date:
2010

Citation for published version (APA):
Habbal, S. R., Druckmüller, M., Morgan, H., Daw, A., Johnson, J., Ding, A., ... Scholl, I. (2010). Mapping the Distribution of Electron Temperature and Fe Charge States in the Corona with Total Solar Eclipse Observations. Astrophysical Journal, 708(2), 1650-1662. https://doi.org/10.1088/0004-637X/708/2/1650

The Astrophysical Journal, 708:1650–1662, 2010 January 10 doi:10.1088/0004-637X/708/2/1650

MAPPING THE DISTRIBUTION OF ELECTRON TEMPERATURE AND Fe CHARGE STATES IN THE CORONA WITH TOTAL SOLAR ECLIPSE OBSERVATIONS

S. Rifai Habbal[1], M. Druckmüller[2], H. Morgan[1], A. Daw[3,4], J. Johnson[5], A. Ding[6], M. Arndt[7], R. Esser[8], V. Rušin[9], and I. Scholl[1]

[1] Institute for Astronomy, University of Hawaii, 2680 Woodlawn Drive, Honolulu, HI 96822, USA; shadia@ifa.hawaii.edu
[2] Faculty of Mechanical Engineering, Brno University of Technology, 616 69 Brno, Czech Republic
[3] Appalachian State University, Boone, NC 28608, USA
[4] NASA Goddard Space Flight Center, Greenbelt, MD 20771, USA
[5] Electricon, Boulder, CO 80204, USA
[6] Institute of Optics and Atomic Physics, Technische Universitaet Berlin and Institute of Technical Physics, Berlin, Germany
[7] Bridgewater State College, Bridgewater, MA 02325, USA
[8] University of Tromsø, Norway
[9] Astronomical Institute, Slovak Academy of Sciences, 059 60 Tatranska Lomnica, Slovak Republic
Received 2009 August 27; accepted 2009 November 23; published 2009 December 23

ABSTRACT

The inference of electron temperature from the ratio of the intensities of emission lines in the solar corona is valid only when the plasma is collisional. Once collisionless, thermodynamic ionization equilibrium no longer holds, and the inference of an electron temperature and its gradient from such measurements is no longer valid. At the heliocentric distance where the transition from a collision-dominated to a collisionless plasma occurs, the charge states of different elements are established, or frozen-in. These are the charge states which are subsequently measured in interplanetary space. We show in this study how the 2006 March 29 and 2008 August 1 eclipse observations of a number of Fe emission lines yield an empirical value for a distance, which we call R_t, where the emission changes from being collisionally to radiatively dominated. R_t ranges from 1.1 to 2.0 $R_\odot$, depending on the charge state and the underlying coronal density structures. Beyond that distance, the intensity of the emission reflects the distribution of the corresponding Fe ion charge states. These observations thus yield the two-dimensional distribution of electron temperature and charge state measurements in the corona for the first time. The presence of the Fe x 637.4 nm and Fe xi 789.2 nm emission in open magnetic field regions below R_t, such as in coronal holes and the boundaries of streamers, and the absence of Fe xiii 1074.7 nm and Fe xiv 530.3 nm emission there indicate that the sources of the solar wind lie in regions where the electron temperature is less than 1.2×10^6 K. Beyond R_t, the extent of the Fe x [Fe^{9+}] and Fe xi emission [Fe^{10+}], in comparison with Fe xiii [Fe^{12+}] and Fe xiv [Fe^{13+}], matches the dominance of the Fe^{10+} charge states measured by the Solar Wind Ion Composition Spectrometer, SWICS, on *Ulysses*, at -43° latitude at 4 AU, in March–April 2006, and Fe^{9+} and Fe^{10+} charge states measured by SWICS on the *Advanced Composition Explorer*, *ACE*, in the ecliptic plane at 1 AU, at the time of both eclipses. The remarkable correspondence between these two measurements establishes the first direct link between the distribution of charge states in the corona and in interplanetary space.

Key words: eclipses – solar wind – Sun: corona

1. INTRODUCTION

The first Fe xi 789.2 nm images of the corona, taken during the 2006 March 29 total solar eclipse, revealed several striking features. Most notable among them were the extent of this emission out to a heliocentric distance of 3 $R_\odot$ and the presence of regions of localized intensity enhancements relative to white light (Habbal et al. 2007a, 2007b). The extent of the emission was attributed to the dominance of radiative over collisional excitation in the Fe xi emission beyond a heliocentric distance of 1.2–1.5 $R_\odot$. The intensity enhancements observed in Fe xi and not in white light, appeared in specific density/magnetic structures in the corona, such as over an active region complex, along the edges and at the cusp of a streamer, and along the neutral sheet above a north–south-oriented prominence. These were evidence for localized Fe^{10+} ion density enhancements. The corona was also imaged in Fe xiii 1074.7 nm during the eclipse of 2006. While this spectral line is also dominated by radiative excitation at larger heights, it displayed fewer examples of localized intensity enhancements, and when present, they were not always co-spatial with those observed in Fe xi.

Imaging the corona in these forbidden lines represents a new direction for exploring the signatures of physical processes responsible for shaping the coronal plasma through the properties of heavy ions. This approach was preceded by space-based observations in the ultraviolet, starting with rocket flights in the early 1970s and the discovery of the Ly α emission in the corona (e.g., Gabriel et al. 1971). The ultraviolet observations in Ly α and the O vi 103.2 and 103.7 nm doublet from the Ultraviolet Coronagraph Spectrometer (UVCS) on the *Solar and Heliospheric Observatory* (*SOHO*; Kohl et al. 1995) led to several discoveries. One of the most noteworthy findings was the realization that heavy ions flow faster than protons in the fast solar wind originating from polar coronal holes starting in the inner corona (Li et al. 1998). Another major discovery was the unexpected large widths in these spectral lines pointing to their response to non-thermal motions in the corona, most likely due to magnetohydrodynamic waves (e.g., Kohl et al. 2006). The novel diagnostic tools provided by these spectral lines were due in part to the significant radiative excitation in their emission. (For coronal Ly α, for example, it is by far the dominant excitation process.) The eclipse observations in 2006 demonstrated for the first time that this was also the case for some of the

spectral lines formed in the visible and near-infrared wavelength range.

Given the novelty and importance of the Fe XI 2006 eclipse results, the goal of the 2008 eclipse observations was to repeat the Fe XI [Fe^{10+}] and Fe XIII [Fe^{12+}] observations and to complement them with observations in Fe X 637.4 nm [Fe^{9+}] and Fe XIV 530.3 nm [Fe^{13+}]. We show how this complement of spectral line imaging leads, for the first time, to the empirical determination of the radial distance R_t at which the transition from a collision-dominated excitation to a radiative excitation of these lines occurs. Consequently, a map of the Fe charge states in the corona out to a heliocentric distance of 3 $R_\odot$ and a map of the electron temperature below R_t are produced. Coupled with the corresponding in situ charge state measurements from the Solar Wind Ion Composition Spectrometers (SWICS) on *Ulysses* (Gloeckler et al. 1992) at high latitudes and on the *Advanced Composition Explorer* (*ACE*; Gloeckler et al. 1998) in the ecliptic plane, the link between the coronal and in situ plasmas is established unambiguously.

We first describe the eclipse experiments (Section 2). The image processing tools (Section 3) used to reveal the topology of coronal structures as seen in white light and in the four Fe lines (Section 4) are given next. In Section 5, we describe how these observations can yield the locus of the transition from a plasma dominated by collisions to a weakly collisional state. Maps of the distribution of the electron temperature and charge states are described in Section 6, with implications for the thermodynamics of the coronal plasma given in Section 7. Concluding remarks given in Section 8 emphasize the uniqueness of eclipse observations as diagnostic tools for the coronal plasma and the sources of the solar wind.

2. DATA ACQUISITION AND CALIBRATION

Details of the data acquisition and calibration for the 2006 eclipse are given in Habbal et al. (2007a). The 2008 August 1 eclipse observations were made by two teams. Team 1 led by S. Rifai Habbal observed the eclipse from the Gobi AlaShan desert in western China. The site was at an elevation of 1342 m and located at N40°23′37.″4 and E99°14′42.″4. The eclipse lasted 1 minute 49.7 s from 11:13:17 to 11:15:06 UT. There were scattered clouds in the sky but none were within the field of view of the instruments during totality. The Czech–German–Slovak Team 2, led by M. Druckmüller and P. Aniol, observed the eclipse from Bor Udzuur in the Gobi desert in western Mongolia, at an altitude of 1223 m, about 23 km southwest of the small village of Altaj, at N45°23′15.″06 and E92°06′50.″22. Totality at that site occurred about ten minutes earlier and lasted for 2 minutes 4 s, from 11:03:35 UT to 11:05:39 UT, under clear sky conditions.

Team 1 imaged the corona in the Fe X, Fe XI, Fe XIII, and Fe XIV nm lines, using thermally controlled narrow (0.5 nm) bandpass filters mounted in front of the objective lenses, and two thermoelectrically cooled PIXIS 1024 × 1024 array cameras manufactured by Princeton Instruments. The cameras have 13 μm pixels and operate at −70 C. Model 1024BR (Camera 1), with a quantum efficiency (QE) of 87% at 789 nm, was ideally suited for the Fe XI 789.2 nm observations. While it was also used for the Fe XIII observations, its QE was around 10% at 1074.7 nm. Model 1024B (Camera 2) was used for the Fe X and Fe XIV lines with a QE of 95% and 96%, respectively, at these wavelengths. The design of the filter holder enabled the interchange of two filters on each camera system during the observing program. A custom-made system using a Thorlabs AC508-300-B near infrared achromatic doublet lens, with a focus shift to optimize for the Fe XI and Fe XIII lines during the observation sequence, was used with Camera 1, and a 300 mm focal length Nikon lens was used with Camera 2. To achieve optimal spectral response, the temperature of the filters was controlled very close to 32 C throughout the observing period. The two optical systems yielded a spatial resolution of 8″ per pixel and a field of view a little over 8 $R_\odot$, or approximately 4°, across the detector. Both camera systems were mounted on the same equatorial mount tracking the Sun.

Given the time constraints imposed by totality, care was taken to choose a suitable set of exposure times that would capture the maximum heliocentric distance possible using the longest exposures, whilst avoiding saturation at low heights with the shortest exposures. Since observations within each filter bandpass consist of contributions from the spectral line and underlying continuum, the observing sequence included measurements with the filters tilted by individually selected angles all near 7° to isolate the intensity of the continuum in the neighborhood of each spectral line. The nominal wavelengths at the tilt angle were 636.3, 787.86, 1073, and 529.4 nm, respectively, for the Fe X, XI, XIII, and XIV associated continua. The sequence of exposure times of 0.5, 2, 4, and 8 s was used for both normal incidence (or onband) and 7° to normal (or offband) measurements. For each spectral line, dark exposures with the shutter closed were obtained for the same exposure times, as well as flat field (i.e., sky) exposures and corresponding darks. For each exposure time, the dark exposures were subtracted from the corresponding set of onband and offband exposures, and then divided by the normalized average of the flat fields. The corrected onband and offband exposures were then divided by their corresponding exposure times. The resulting onband and offband exposures were then subtracted from each other to yield images in the corresponding spectral lines.

The co-alignment of the images from different exposure times (for both spectral line and corresponding continuum) was first done manually and then checked by using a Fourier transform method (as described by Druckmüller et al. 2006). Images were rotated to place solar North vertically up. A simple weighting method was then used to combine images taken with different exposure times. At the shortest radial distances, a given image is dominated by the 0.5 s exposure. As the distance increases from 1 to 1.15 $R_\odot$, there is a gradual increase in weighting from the 0.5 s to the 2 s exposure such that at 1.15 $R_\odot$ the image is dominated by the 2 s exposure. Between 1.15 and 1.25 $R_\odot$, there is a ramping from the 2 s to the 4 s exposure. A similar ramping ensures that by 2 $R_\odot$, the image becomes dominated by the 8 s exposure. The ramping is nonlinear, and at some radial distance the output image may be composed of different weightings from three different exposure times. This simple method ensures a smooth transition in brightness between different regions of the corona as observed with different exposure times. A simple scheme is applied where an increasing level of sliding window median smoothing occurs with increasing distance to help reduce noise. The sliding window is 5 × 5 pixels. The final image consists of the non-smoothed image at low heights ($\leqslant$1.1 $R_\odot$), the smoothed image only at large heights ($\geqslant$3 $R_\odot$), and a height-weighted sum of non-smoothed and smoothed images between these two heights.

The Czech–German–Slovak Team 2 observations concentrated on high spatial resolution white light and Fe XIV (530.3 nm) imaging (see Pasachoff et al. 2009, for details). For the white light, several cameras with different focal length

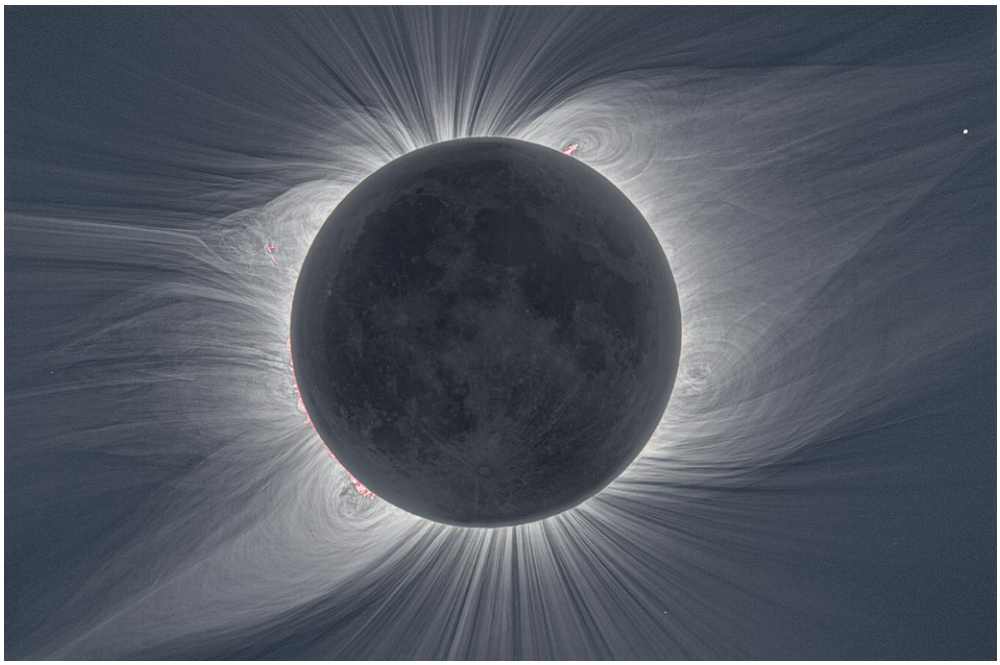

Figure 1. High spatial resolution white-light image of the corona from the 2008 August 1 eclipse, taken by Team 2 with a series of exposure times and DRM processed.

lenses were mounted on the same solar tracking mount, and controlled by specially designed Linux software. A total of 255 exposures were taken, ranging from 8 s to 1/4000 of a second. Imaging in Fe XIV was done using identical 500 mm, $f/8$ lenses with two Canon EOS 5D cameras. Each camera was retrofitted with a 0.15 nm narrow-passband filter, manufactured by Andover Corporation, which was placed between the camera body and the objective lens. One of the filters was centered on Fe XIV, and the other at 529.1 nm line in the neighboring continuum. Both filters were manufactured for an optimal spectral response at 45 C. The spatial resolution was 4″ per pixel. (Because of the higher spatial resolution of these Fe XIV observations compared to Team 1's, they will be used in the analysis to follow.) Twelve exposure times, ranging from 1 to 8 s (ISO 400), including one at 8 s with ISO 800 and one at 8 s with ISO 1600, were taken. The images were calibrated with dark frames and flat-field exposures and aligned by means of phase correlation. The Fe XIV emission line was then extracted from the subtraction of the calibrated images in these two filters. With such a setup, there were no potential ambiguities associated with non-normal incidence for the continuum exposures. The images with different exposure times were then combined into a single 64 bit pixel^{-1} high dynamic range image with linear brightness scale using a specially designed (LDIC 5.0) software.

3. IMAGE PROCESSING

The topology of the corona in broadband white light, and in the spectral lines used, is best revealed by the application of image processing tools. Two methods were used: The Normalizing Radial Graded Filter, or NRGF, developed by Morgan et al. (2006) and the novel method developed by Druckmüller et al. (2006), or DRM hereafter. (See also Druckmüller 2009). Both approaches compensate for the steep radial fall off of the intensity of the coronal emission, hence for its high dynamic range, and enhance the sharp gradients in latitude inherent to coronal structures, without introducing any spurious artifacts in the images. The quantitative analysis, though, is carried out with the unprocessed data.

The NRGF allows comparison of structure at all heliocentric distances within a coronal image by removing both the steep radial gradient in brightness and the brightness variation. It does this by calculating the average and standard deviation of brightness as a function of the heliocentric distance, then by subtracting the average and dividing by the standard deviation at each pixel. Throughout the NRGF-processed image each height then has an average of zero brightness and unity variation. This is an effective and correct method to reveal coronal structure without introducing large-scale artifacts.

The DRM method is based on adaptive filters akin to human vision, which suppress low spatial frequencies and amplify high spatial frequencies. The filters used to modify the frequency characteristics of the image do not change the Fourier phase spectrum. The filter has circular frequency characteristics on high spatial frequencies, i.e., it behaves identically in all directions. This approach is far more comprehensive than existing methods which have non-circular frequency characteristics, such as the radial unsharp masking (often called radial filter). The latter enhances only the radial structures while the tangential structures are suppressed, thus quenching coronal structures involving loops. The DRM approach enhances coronal structures equally in all directions. Hence, the extreme brightness gradient in the solar corona in the radial direction is reduced without introducing any processing artifacts.

4. TOPOLOGY OF THE CORONA

4.1. The Corona as Seen in White Light

Shown in Figure 1 is the 2008 composite broadband white-light image of the corona. Application of the DRM image processing reveals structures at a spatial resolution of 1 arcsec. The ubiquitous filamentary nature of coronal density structures is most evident in the plumes in the polar regions. They extend to the edge of the field of view of the image, out to at least 1 $R_\odot$ above the limb. Streamers appear with intricate loop-like, sometimes twisted, structures at their base. These loops overlay prominences which appear as pinkish structures

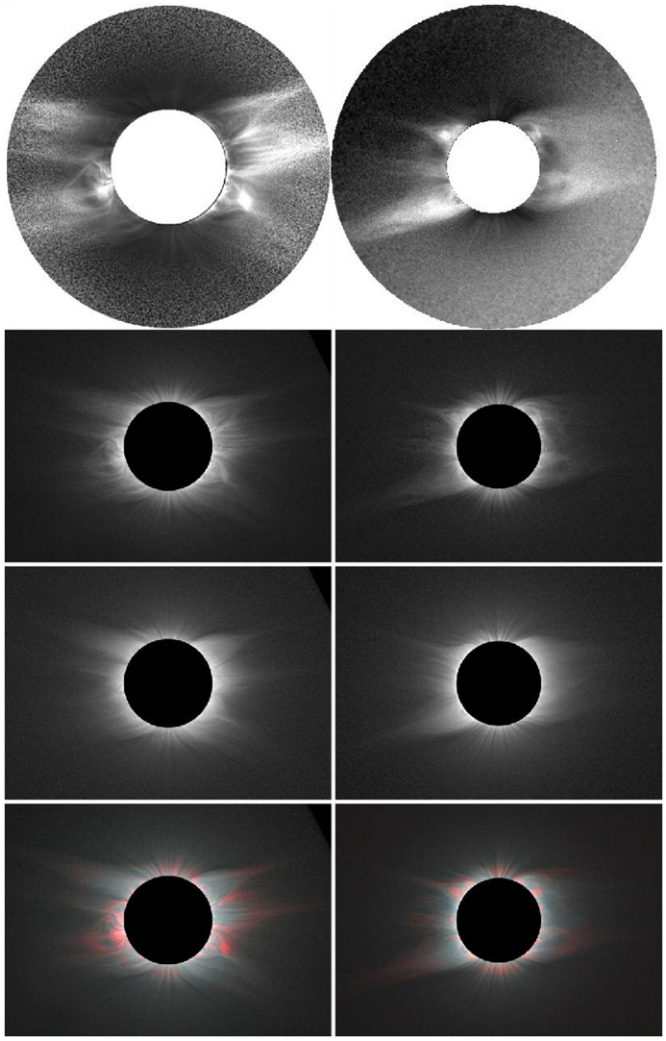

Figure 2. Fe XI images of the corona taken during the eclipses of 2006 March 29 (left columns) and 2008 August 1 (right columns). In the top two panels the images were processed with the NRGF. Note that the two scales are not the same: the effective field of view in 2008 was larger due to higher signal-to-noise as a result of improved optics. The following six panels were DRM processed. The first two are the Fe XI line, followed by the corresponding continuum. An overlay of the line to continuum, with the red indicating regions of enhanced Fe relative to white-light emission is shown in the bottom panels.

due to the dominance of their Hα emission. There are also density structures that seem to arch across the more well-defined streamers. Although solar minimum persisted from 2006 to 2008, with very few emerging sunspots, the distribution of streamers at these two eclipses was not limited to the equator. For example, in 2008 there were four well-defined streamers (two on the east limb and two on the west) similar to the more classical shape of a helmet streamer gradually tapering off with distance. Such a distribution is likely due to a quadrupolar component of the large-scale magnetic field shaping the corona.

4.2. The Corona as Seen in Fe XI Emission

Shown in the top two panels of Figure 2 are the Fe XI NRGF-processed images from 2006 (left columns) and 2008 (right columns). (Improvement in the optics in 2008 yielded a higher quality Fe XI image when compared to 2006.) The same striking Fe XI characteristics, first seen in 2006, also appeared in 2008, namely, (1) an emission extending out to at least 2 $R_\odot$ above the limb in streamers and (2) the appearance of regions of localized intensity enhancements.

The corresponding DRM-processed Fe XI images are shown in rows 2–4 in Figure 2. The first set (second row) is the line emission, and the second set (third row) is the neighboring continuum. The bottom panels correspond to the ratio of the spectral line to continuum. While NRGF brings out the details of large-scale structures, the DRM processing reveals intricate filamentary structures in the emission, not limited to the polar plumes. By comparing the Fe XI emission (second row) to the continuum (third row) it becomes clear that coronal structures seen in Fe XI are far more intricate than in the continuum recorded with the same optical system. This is somewhat surprising given that one expects the continuum emission resulting from the scattering of photospheric radiation by coronal electrons to reveal all density structures, as opposed to the inherent limitations of spectral line emission given its dependence on the underlying physical properties of the corona, such as temperature, elemental abundance, and ion density.

The enhanced ratio of Fe XI line to continuum intensities is seen in red in the DRM-processed images in the bottom panels when the falloff with distance of the Fe XI intensity is slower than that of the continuum. These correspond to the same regions detected visually in the NRGF-processed images (top row). As such they provide evidence that these enhancements correspond to Fe^{10+} ion density enhancements relative to electron densities, as first reported by Habbal et al. (2007a). In comparing the 2006 and 2008 coronal images, there is no obvious magnetic structure which seems to favor, a priori, the location of these enhancements. In the polar regions, the enhancements occur in plumes over a distance range of 0.25 $R_\odot$ starting from the solar surface. In the streamers, they are localized along their boundaries for the most part. As found in 2006, there are regions of enhanced emission within complex magnetic structures that have no clear counterparts in the continuum. Such is also the case for 2008 at position angles, PA (measured counter-clockwise from 0 degrees north), around 45° and 290°. In comparison with the high spatial resolution image of Figure 1, the enhancements in the east streamer are associated with a complex structure surrounding a filament which appears to be suspended at about 0.1 $R_\odot$ above the limb. On the west limb, the enhancement is associated with the southern portion of the large loops surrounding the large filament at PA 320°. In the 2006 Fe XI image, the most dominant enhancements consisted of an unusual bubble in the southeast and the complex streamer structure in the southwest.

4.3. The Corona as Seen in All Fe Lines

To explore the uniqueness of the Fe XI observations, we first compare Fe XI with Fe XIV, which has the strongest emission among the other spectral lines observed, and also represents a much hotter plasma, as will be discussed in more detail in Section 5. Shown in Figure 3 is a sequence of DRM-processed images, namely, the line emission (top), the neighboring continuum (middle), and the ratio of Fe XIV emission to continuum (bottom). This is the same sequence as shown in Figure 2 for Fe XI (i.e., the three lower panels in either column). Unlike Fe XI, the dominant Fe XIV emission seems to be confined to the innermost corona, notably the bases/bulges of streamers. These regions also seem to be the loci of enhanced Fe^{13+} density enhancements relative to electron densities as seen in the green shading of the lower panel. It is clear from the comparison of the lower panels of Figures 2 and 3 that the regions of enhanced ion emission relative to white light are different for the Fe XI and Fe XIV lines.

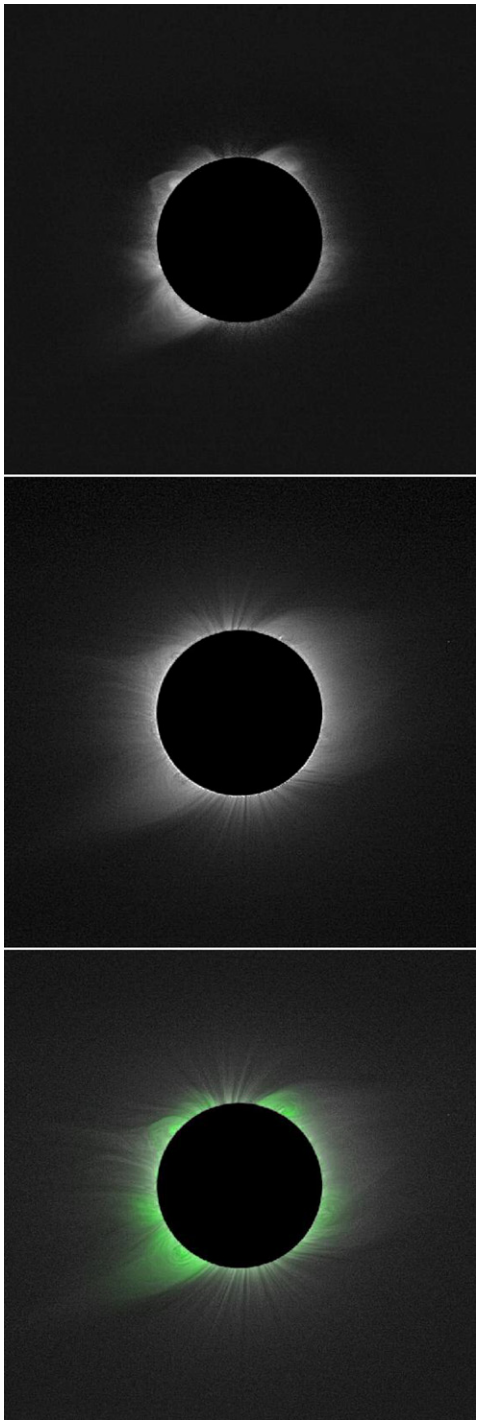

Figure 3. Top: Fe XIV emission; middle: corresponding continuum emission; bottom: overlay of enhanced Fe XIV emission relative to continuum shown in green. All images are DRM processed.

We consider next the topology of the corona as seen in all Fe lines. These are shown in Figure 4, in order of increasing charge or ionization state from top to bottom. In each row, the sequence consists of the NRGF-processed continuum (left panel), the NRGF-processed spectral line (middle panel), and the corresponding DRM-processed spectral line image (right panel). The fields of view do not have the same size since they were truncated when the coronal signal disappeared. It is clear that the most extended emission with significant signal-to-noise ratio appears in Fe XI.

To identify instrumental effects that could potentially impact the comparison of the emission in these spectral lines, we first compare the continuum images. These should yield the same large-scale structures. This is indeed the case, as seen in the left panels of Figure 4 where the large-scale structures are indistinguishable. The weaker Fe XIII-associated continuum emission is a result of the low QE of the detector at this wavelength. Given the excellent correspondence of the large-scale structures between these continuum images, any detected differences in the corresponding line emission are therefore real and cannot be instrumental.

Inspection of the 2008 observations in Figure 4 shows that there is a strong resemblance in coronal structures between Fe X and Fe XI, and between Fe XIII and Fe XIV. In particular, there is a clear demarcation between these two pairs of lines in the polar regions, and within streamers and their extension. The polar plumes are brightest and most extended in Fe X and Fe XI, while only their bases are seen in Fe XIII and Fe XIV, most likely reflecting emission from bright points there. Within streamers, the Fe XIII and Fe XIV emissions dominate the lower heights, while the emission from Fe XI, and Fe X to a lesser extent, span larger distances. The same trend had been seen in the 2006 Fe XI and Fe XIII observations. Since the latter have been described in detail in Habbal et al. (2007a), we concentrate in what follows on the details of the 2008 streamer observations which are identified by numbers in Figure 4.

Streamer 1 consists of two closely connected structures, the complexity of which is clearly seen in the high-resolution white-light image of Figure 1. The southern part is dominated by Fe XI emission starting almost at the coronal base; the northern structure is best seen in Fe XIII/Fe XIV. The suspended prominence noted earlier in Figure 1 seems to define the boundary between the two. The extension and tapering of the streamer is observed only in the weaker Fe X and the prominent Fe XI emission.

The complex structure labeled 2 at the east limb is akin to a twisted streamer seen edge-on. It is likely to be of the type referred to by Morgan & Habbal (2007) as fan streamers which twist to a more face-on alignment further away from the Sun. Emission in all lines is observed at the base of this structure in both NRGF and DRM processing. However, its extension is only observed in Fe X and Fe XI, with a localized enhancement observed in Fe XIV at its base (see Figure 3).

Streamer 3 displays the more classical helmet configuration; observed face-on it appears in all wavelengths. The details of its underlying structure, and its extent, are best visible in Fe XI and Fe XIV. Streamer 4 seems to have the same topology, yet no emission in Fe XIII or Fe XIV is detected beyond its base. Its extension in Fe XI is quite remarkable. Such is also the case for streamer 6.

The region labeled 5 is very faint in Fe XIII and Fe XIV, and shows no extension in Fe XI. There is a thick loop-like structure overarching it observed only in Fe XI, again seen in both NRGF and DRM processing.

The spatial correspondence between the four Fe lines is best seen in the color overlays of Figure 5 where Fe XI emission is shown in red, Fe XIII in blue, and Fe XIV in green. To reduce clutter, Fe X has been omitted in the 2008 composite because of its very close resemblance to Fe XI. For the 2006 eclipse observations (left panels), the overlay is limited to Fe XI and Fe XIII, since they were the only observed lines. The background white-light emission has been added to the spectral lines in the lower panels.

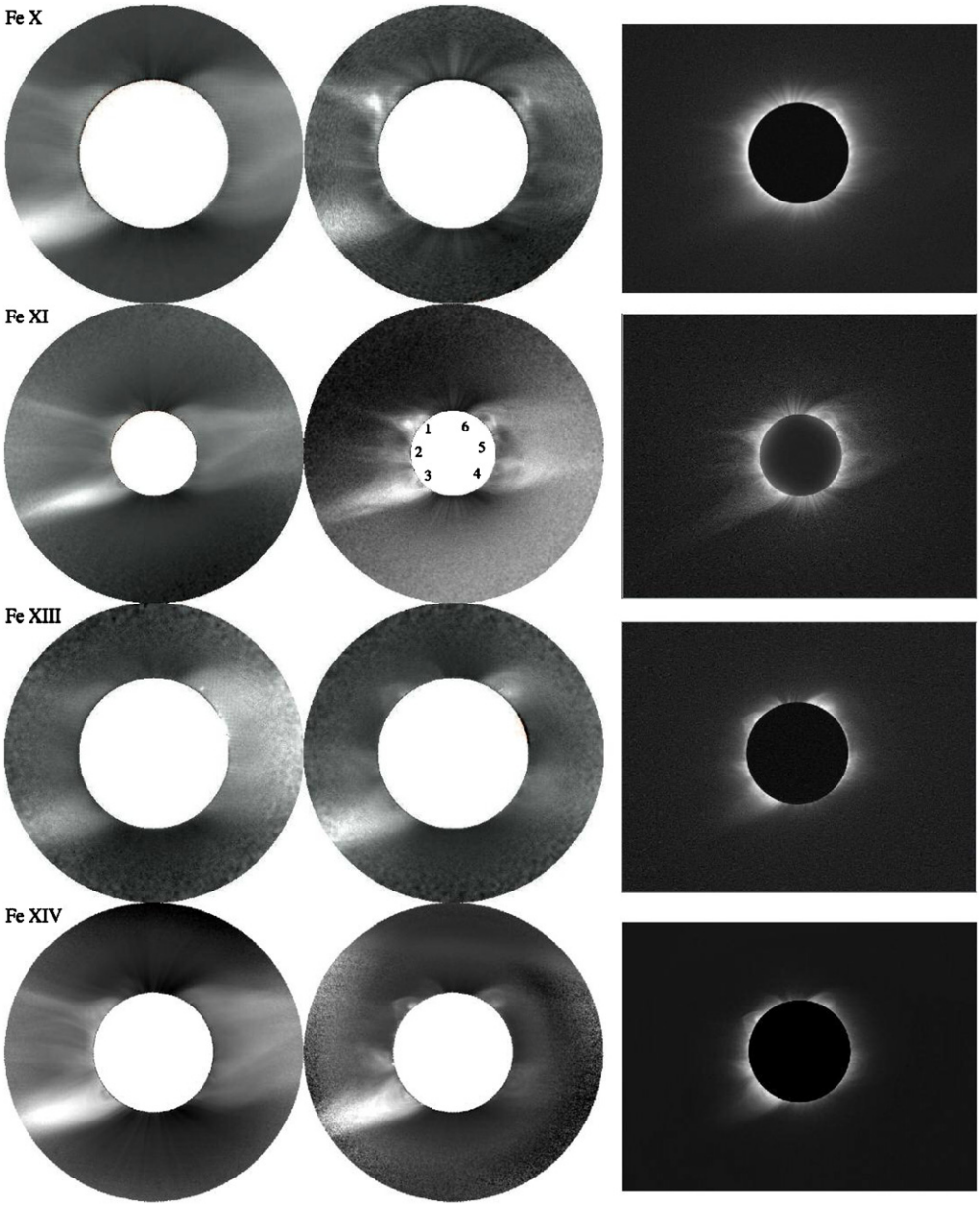

Figure 4. Composite of the four Fe line observations from 2008 August 1. The images are arranged in rows starting with Fe x 637.4 nm [Fe^{9+}] (top), and ending with Fe XIV 530.3 nm [Fe^{+13}] (bottom). In each row, for each spectral line, the left panel is the continuum, the middle one is the spectral line, both NRGF-processed, and the right panel is the DRM-processed spectral line. The displayed field of view in the NRGF images (with the size of the solar/lunar disk indicated in the middle) is truncated differently among the lines depending on the noise level in each spectral line.

In summary, it is clear from the comparison of all Fe NRGF- and DRM-processed images that the underlying details and extent of the large-scale structures in the corona are most evident in Fe XI in comparison with the other wavelengths. The areas of localized enhanced emission, namely the ratio of line to continuum, appear in the polar regions and the expanding corona along the boundaries of streamers in Fe XI, but are confined to the bulges of streamers in Fe XIV, with almost no overlap between the enhanced emission in these two spectral lines.

5. INFERENCE OF THE TRANSITION FROM A COLLISIONAL TO A COLLISIONLESS PLASMA IN THE CORONA

The observed differences—and similarities—between the four Fe lines and white light can be accounted for by considering two basic properties: (1) the role of the electron temperature in the formation of these lines and (2) the relative contribution of collisional and radiative excitation to their emission.

We consider first the role of the electron temperature. Shown in Figure 6 is a plot of the ion fraction for Fe x through Fe XIV (Fe XII is included for completeness, but does not factor in the observations). This plot also gives the peak electron temperature at the maximum ion fraction for a given line, namely, 0.94×10^6 K for Fe x, 1.16×10^6 K for Fe XI, 1.59×10^6 K for Fe XIII, and 1.82×10^6 K for Fe XIV. These figures were derived from the CHIANTI database using values given by Mazzotta et al. (1998) and assuming thermodynamic ionization equilibrium. As shown by Esser et al. (1998), even if the Fe ions have an outflow velocity, this has little effect on these curves.

It is clear that Fe XIII has the largest ion fraction and Fe XIV the lowest. While the temperatures for maximum ionization are

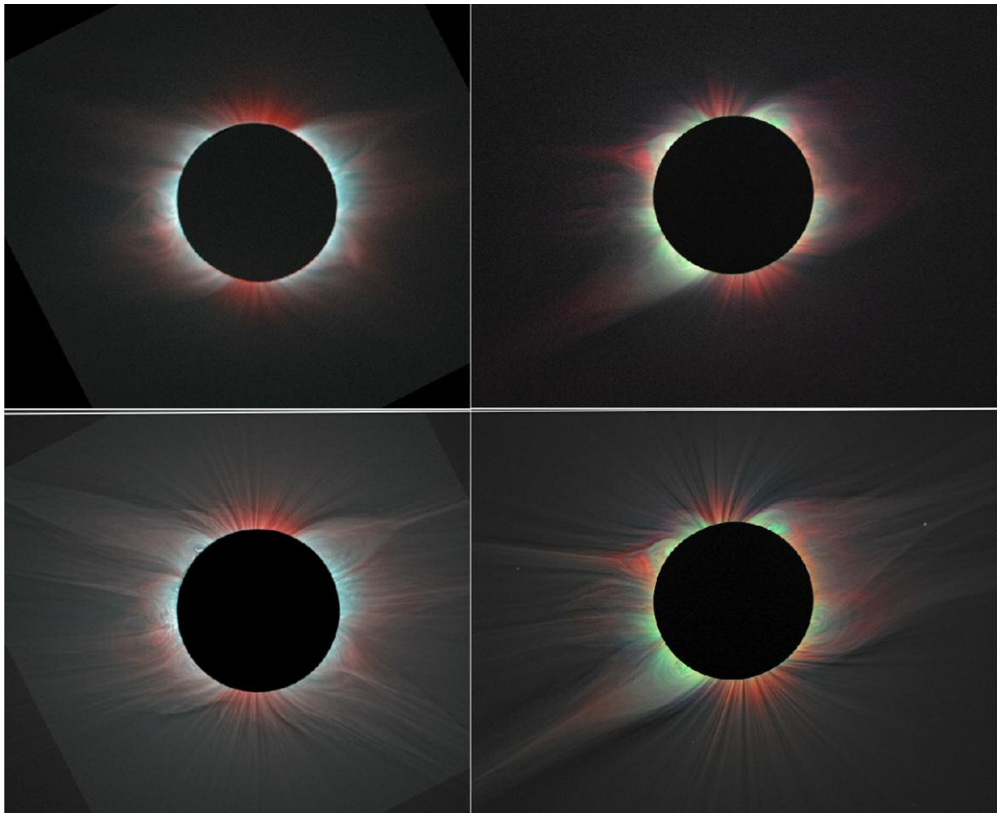

Figure 5. Color overlay of the emission from all Fe lines (top panels) and combined with white light (bottom panels). The left column corresponds to the 2006 eclipse observations, which were available only in Fe XI (red) and Fe XIII (blue). In 2008 (right column), Fe XI is shown in red, Fe XIII in blue, and Fe XIV in green. Fe X is not included because its emission closely replicates that of Fe XI, albeit much weaker, hence with a more limited extent in radial distance.

different, there is a significant overlap between neighboring charge states, with the largest overlap between Fe XIII and Fe XIV. Hence, from the standpoint of the electron temperature, one expects the corona to look very similar in Fe X and Fe XI, and in Fe XIII and Fe XIV. Several features already discussed in Figures 3 and 4 support this prediction.

We consider next the relative contribution of collisional and radiative excitation to the emission. As noted earlier by Habbal et al. (2007a), and shown in their Figure 7, radiative excitation is far more dominant in the formation of the Fe XI line in comparison with Fe X and Fe XIV for a wide range of relevant coronal electron densities and temperatures. Model calculations by Judge (1998) show that the radiative component for Fe XIII is likely to be even larger than for Fe XI.

Habbal et al. (2007a) showed how the ratio of the line to continuum could be used as a proxy for determining the transition from the dominance of collisional to radiative excitation in the emission process (see examples in their Figures 8 and 9). The argument is as follows. When collisions dominate the emission process, the intensity of a spectral line is proportional to the product of the electron and ion densities. For radiative excitation, on the other hand, the intensity is proportional to the ion density. (We ignore dependences on other parameters such as abundance and temperature since they contribute to both processes in the same manner). The intensity of the continuum is proportional to electron density. Hence, to first order, the ratio of line to continuum will be proportional to the ion density for collisionally dominated excitation, and to the ratio of ion-to-electron density when dominated by radiative excitation. If the falloff of ion and electron densities with the radial distance is the same, this ratio should be constant when radiative excitation dominates. Consequently, the ratio of line to continuum through any structure as a function of the radial distance should have a sharp drop-off close to the Sun, when collisional excitation dominates, and should become flat past a given radial distance when radiative excitation becomes the dominant process. The change in the slope then yields the radial distance at which the transition to a radiatively dominated emission occurs. We refer to this distance as R_t.

One can apply this empirical approach to produce a contour of R_t in the two-dimensional images of the corona. This contour is overlayed in Figure 7 over the corresponding Fe X, Fe XI, Fe XIII, and Fe XIV NRGF-processed images. To produce this contour, it is necessary to apply considerable smoothing. An 11×11 pixel (around $0.1\ R_\odot$ square) sliding window median filter is applied to the onband and offband images. This removes any spikes and helps reduce the salt and pepper noise. A 5×5 pixel sliding window average smoothing is then applied. The line is then calculated as a subtraction of the offband from the onband. The line and continuum images are rebinned into polar coordinates, with 360 position angle bins and 40 height bins between 1 and $3\ R_\odot$, and the ratio of the line to the continuum and the height differential of the ratio are calculated. The latter is large close to the Sun, corresponding to the steep decrease of the ratio (owing to the line intensity dropping more steeply than the continuum). The differential drops to values close to zero with increasing height, indicating one of two cases: that the intensity of the spectral line has reached a point where it decreases at the same rate as the continuum (that is, the radiative component has become dominant), or that it is practically zero. It is simple to decide which case is true by looking at the NRGF-processed image, set as the background image to the contours of Figure 7.

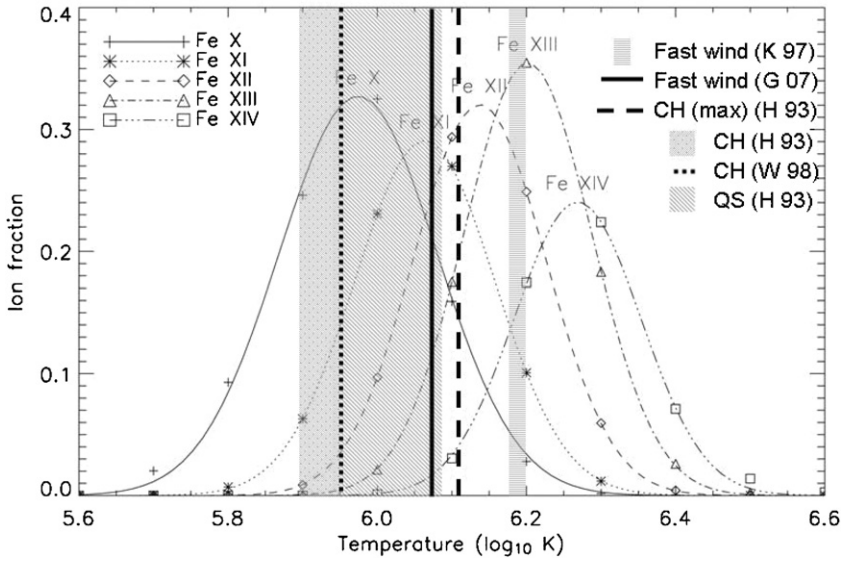

Figure 6. Ion fraction as a function of log electron temperature for all four Fe lines, calculated using the CHIANTI database and assuming ionization equilibrium. Fe XII is included for completeness, but is not an observed spectral line in the visible. The dotted shading covers the coronal hole temperature range of 0.8 to 0.9 × 10^6 K (log T = 5.9–5.95) and the diagonal shading corresponds to the quiet-Sun temperature range of 0.9–1.2 × 10^6 K (log T = 6.08) at the boundaries of a polar coronal hole, both inferred by Habbal et al. (1993) from 1.02 to 1.07 $R_\odot$. The dashed line is the upper limit of the coronal hole temperature of 1.3 × 10^6 K (log T = 6.11) at 1.6 $R_\odot$ derived from a curve fit to different data by Habbal et al. (1993). The dotted line is at T = 0.9 × 10^6 K (log T = 5.95) for the distance range of 1.03 to 1.6 $R_\odot$ inferred by Wilhelm et al. (1998). The solid line corresponds to the in situ fast solar wind freeze-in temperature of 1.18 × 10^6 K (log T = 6.07) inferred by Gloeckler & Geiss (2007) from 3 years of *Ulysses* data at solar minimum. The horizontal shading covers the freeze-in temperature range of 1.5–1.6 × 10^6 K (log T = 6.18–6.2) over 1.3–1.5 $R_\odot$ derived by Ko et al. (1997) in the fast wind during the first *Ulysses* south polar pass.

The contour is placed at a value where the steep gradient ends, and the differential comes close to zero. The height uncertainty is around 0.1 $R_\odot$ depending on position in the image (i.e., in some places, the point where the collisional component disappears is easier to pinpoint than others). However, the smoothness, or consistency of the contour across position angles, testifies to the correctness of the analysis.

As shown in Figure 7, the contours of R_t are similar for Fe X and Fe XI, but are different from the Fe XIII and Fe XIV contours. The Fe XIII contour has a greater uncertainty than the others, as evident in the irregularity of its shape (a consequence of the low QE of the detector as noted earlier). Overall, R_t ranges between 1.1 and 2 $R_\odot$. While the Fe X and Fe XI emissions extend past their respective R_t contour, the Fe XIV emission stops there with the exception of the southeast streamer.

The transition from collisional to radiative excitation also indicates the transition from a collisional to a collisionless regime in the coronal plasma, which has direct implications for the observed charge states in the corona. In fact, an optimal combination of electron temperature and density, conducive to frequent collisions, will enable the ionization of an element up to a given charge state, as shown in Figure 6. Once the electron density drops to a level where collisions become infrequent, and collision timescales become small relative to the expansion timescale (defined as $(n_e/v_i)(dn_e/dr)^{-1}$, where n_e is the electron density and v_i is the ion outflow velocity), an ion with a given charge state is unlikely to change identity (see Hundhausen 1968), a state commonly referred to in the literature as "frozen-in." It is therefore very likely that the freezing-in location is closely associated with the distance we defined as R_t.

These multiwavelength eclipse observations thus lead to the first empirical determination of the locus of the transition between a collision-dominated regime to a collisionless one for a given ion emission line, and the locus of its departure from ionization equilibrium in the corona. Below R_t, collisions dominate the emission process and the distribution of the emission in the different spectral lines reflects the distribution of electron temperature in the corona. Beyond R_t the charge state of a given Fe ion becomes "frozen-in," and the distribution of the emission reflects the distribution of the charge states. To the best of our knowledge, this is the first empirical inference of this critical distance.

6. MAPS OF THE DISTRIBUTION OF ELECTRON TEMPERATURE AND FE CHARGE STATES IN THE CORONA

One of the unique features of the multiwavelength eclipse observations is the two-dimensional distribution of the emission in the inner corona, starting from the solar surface out to a few solar radii. With the identification of the empirical range of R_t values shown in Figure 7, the two-dimensional distribution of the electron temperature and Fe ion charge states in the corona can thus be inferred for the first time, as described in more detail below.

6.1. Electron Temperature Distribution

The electron temperature in the corona is commonly derived from the intensity ratios of collisionally excited spectral lines observed in the extreme ultraviolet (EUV), which are typically limited to heliocentric distances below 1.5 $R_\odot$. By applying this technique to EUV data from Skylab acquired in 1973, Habbal et al. (1993) derived a temperature range of 0.8–0.9 × 10^6 K in a polar coronal hole and a range of 0.9–1.2 × 10^6 K in its neighboring quiet region, off the limb from 1.02 to 1.07 $R_\odot$. By complementing these inferences with compilations from other techniques, these authors also provided an empirical curve for the temperature gradient starting around 0.8 × 10^6 K at the solar surface and reaching a maximum slightly below 1.3 × 10^6 K at 1.6 $R_\odot$. The inference by Wilhelm et al. (1998) for more recent coronal hole observations of differ-

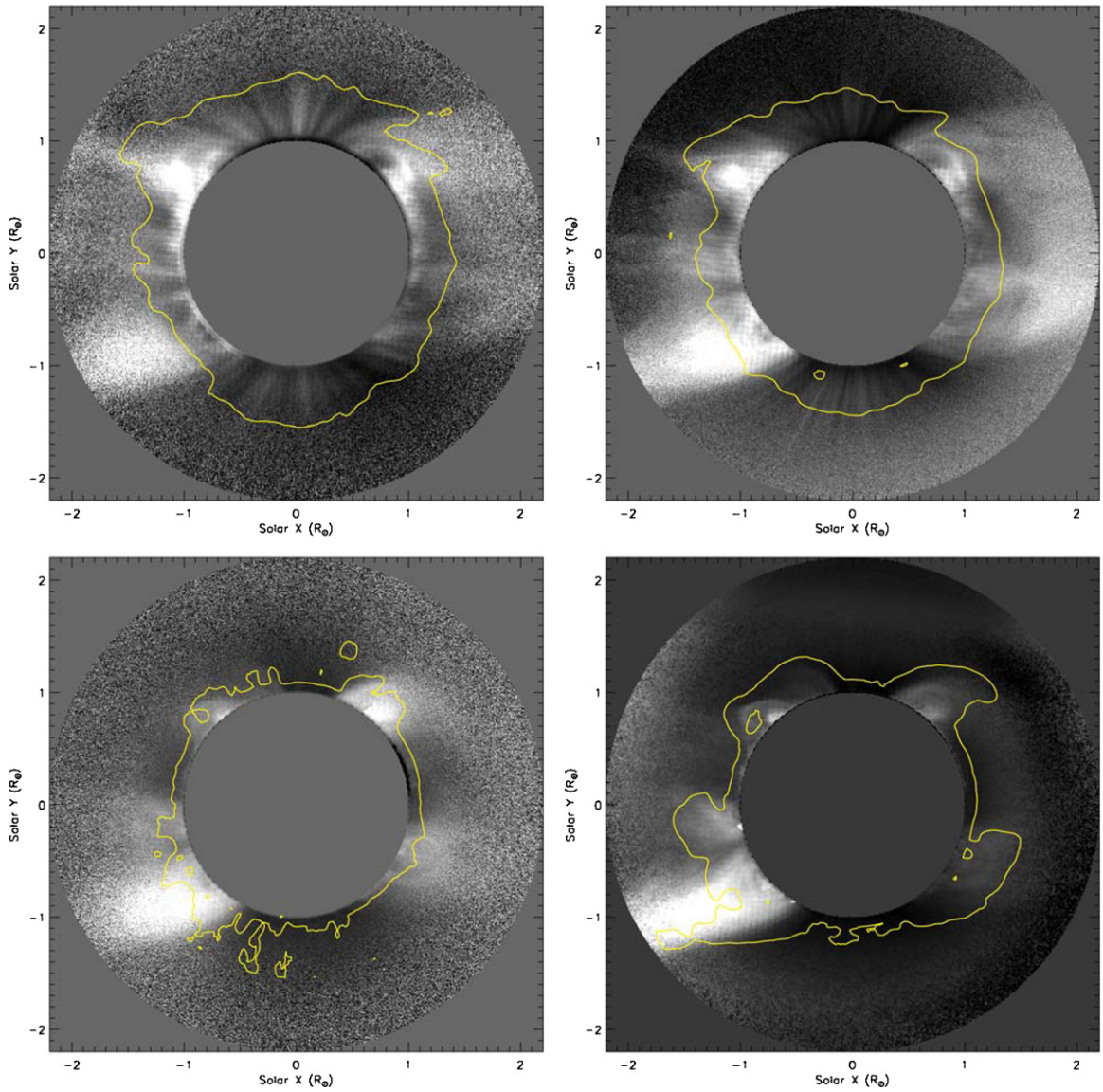

Figure 7. Contours of R_t overlayed on the Fe X (top left), Fe XI (top right), Fe XIII (bottom left), and Fe XIV (bottom right) 2008 eclipse NRGF-processed images.

ent Mg lines from Solar Ultraviolet Measurement of Emitted Radiation, SUMER/SoHO, led to a temperature of 0.9×10^6 K over the distance range of 1.03–1.6 $R_\odot$ in very close agreement with Habbal et al.'s inference below 1.07 $R_\odot$. The temperature ranges derived from these two studies are shown superimposed on the ion fraction curves of Figure 6.

Here we infer the electron temperature from the observed distribution of the emission (Figures 5) and the use of the ion fraction curves (Figure 6), and not from the ratio of spectral lines. As noted earlier in Section 4.3, there seems to be a clear demarcation between emission in Fe X/Fe XI and Fe XIII/Fe XIV for most coronal structures. Reference to Figure 6 implies that the electron temperature is in the range of $0.8–1.2 \times 10^6$ K when Fe X and Fe XI emission dominates (namely the temperature range between their peak formation temperatures or slightly below) when Fe XIII and Fe XIV emission should be absent. Similarly, when only Fe XIII and Fe XIV emission are observed, the temperature is in the range of $1.6–2.2 \times 10^6$ K (i.e., in the range of their peak formation temperatures or slightly above) to exclude Fe X and Fe XI emission. There are, however, structures where emission from all lines is present, reflecting a multi-thermal plasma in that case. We note that no radial temperature gradient can be derived from these eclipse observations with the simple approach considered here.

In both 2006 and 2008, there is a distinct dominance of the cooler Fe X and Fe XI emission in the polar regions, or polar coronal holes (red shading in Figure 5). This corresponds to a temperature range of $0.8–1.2 \times 10^6$ K, which is comparable to that inferred by Habbal et al. (1993) and Wilhelm et al. (1998). (The Fe XIII and Fe XIV emission observed very close to the coronal base, as seen in the shades of green and blue in Figures 4 and 5, is most likely indicative of the presence of coronal bright points at the base of coronal holes, as noted earlier.) In closed magnetic structures forming the base of streamers, the emission is dominated by Fe XIII (in 2006 and 2008) and Fe XIV (in 2008) as seen in Figure 5, hence characterized by plasma temperatures in the range of $1.6–2.2 \times 10^6$ K.

While two distinct temperature structures dominate the two eclipse observations, there are exceptions. One such example is the streamer labeled 3 in Figure 4. Although the base of the streamer is very different in the cooler Fe X and Fe XI lines than the hotter Fe XIII and Fe XIV lines, its extension is observed in all

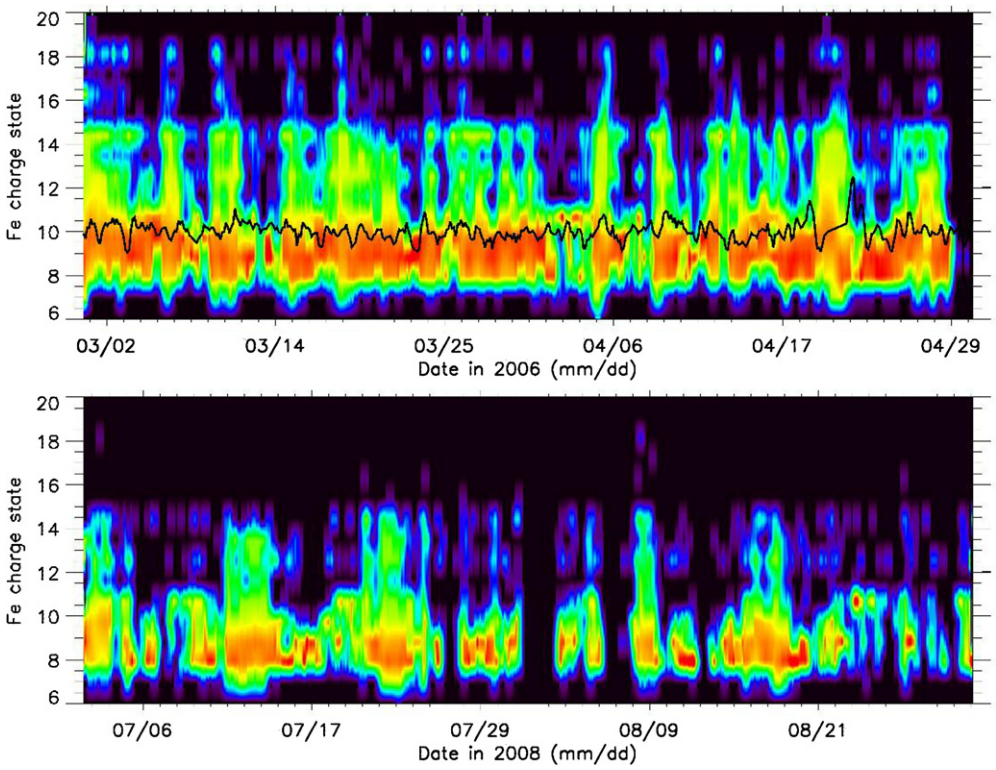

Figure 8. Top plot shows 15-hr averages of the *ACE* SWICS Fe charge state measurements taken over a period of ± 30 days centered on the 2006 eclipse date. (*ACE* was in the ecliptic plane at 1 AU). Black regions represent either a very low signal, or missing reduced data (usually due to low signal). Red shows the most dominant charge states, with intermediate colors ascending purple, blue, green, and yellow. The black line shows the 15-hr average Fe charge state measured by *Ulysses* over the same period. Note that the *Ulysses* data are average charge states, unlike the *ACE* data that are the individual charge states. During this time period, *Ulysses* was at −43° latitude at a distance of 4 AU. The bottom plot shows the 15-hr averaged *ACE* measurements for a period of ± 30 days including the 2008 August 1 eclipse; no *Ulysses* data were available then.

lines, most likely an indication of a multi-temperature plasma. On the other hand, in the streamer labeled 1 in Figure 4 and clearly seen in Figure 5, there is a distinct separation between the cooler and hotter emission lines within the complex magnetic structures at its base. In 2006, a large bubble in the southeast, indicative of a closed magnetic structure, was seen only in the cooler Fe XI line. The region labeled 5 in Figure 4, with an overarching thick loop, was also characterized by the cooler Fe XI line emission.

Figure 5 can thus be regarded as a map of the electron temperature of the corona (upper panels), placed in the context of density structures as represented by white-light emission (lower panels), at the time of the eclipses of 2006 and 2008. These maps indicate that the electron temperature in the expanding corona was dominated by cooler electron temperatures averaging 10^6 K. The expanding corona is not necessarily limited to coronal holes but also encompasses the boundaries of streamers and open structures within and between streamers. The bulges of streamers, on the other hand, are characterized by hotter plasma, i.e., 1.6–2.2 × 10^6 K, emitting preferentially in the Fe XIII and Fe XIV lines.

6.2. Distribution of Fe Charge States

As mentioned earlier, each spectral line has a characteristic R_t curve. At distances beyond R_t, the emission reflects the distribution of its corresponding charge state. For 2006, when observations in Fe XI and Fe XIII only were available, the extent of Fe XI emission in comparison with Fe XIII, as shown in Figure 4, implies a dominance of Fe^{10+} charge states in the expanding corona. In 2008, the emission beyond R_t was limited to Fe X and Fe XI, with the exception of streamer 3. Hence the spatial distribution there reflects the spatial distribution of Fe^{9+} and Fe^{10+} ions. The extent of the emission in all four lines within streamer 3 beyond R_t as shown in Figure 7 is an indication that all charge states are present there.

The only charge state measurements available for comparison are those from interplanetary space. To date, the most comprehensive data set is from the SWICS on *Ulysses* (Gloeckler et al. 1992) and *ACE* (Gloeckler et al. 1998). *ACE* is restricted to the ecliptic plane at 1 AU, while *Ulysses*, which stopped returning charge state measurements in early 2008, was at −43° latitude around 4 AU during the 2006 eclipse measurements. Shown in Figure 8 are the 15-hr averages of *ACE* Fe charge state measurements over a ± 30 day period surrounding the 2006 and 2008 eclipse dates. Black regions represent either a very low signal, or missing data (usually due to low signal). The colors of purple, blue, green, and yellow give the charge states in ascending order, with red representing the most dominant charge states. The black line is the 15-hr average of the average Fe charge state at any given time measured by *Ulysses* over the same period. We note that the publicly available *Ulysses* data are averages over the charge states. Hence information about the full distribution of charge states, such as the high charge states of say Fe^{16+} present in the *ACE* data, is absent in the *Ulysses* data shown here.

It is clear from these measurements that the dominant charge states in interplanetary space encompassed Fe^{8+} to Fe^{10+} during the periods covering both eclipses. Hence, the dominance of Fe^{10+} in the corona during the 2006 and 2008 eclipses and the additional detection of Fe^{9+} in 2008 coincide remarkably

well with the dominant charge states measured in situ by both spacecraft. The occasional presence of higher charge states, such as Fe^{11+} to Fe^{16+} as measured by *ACE*, and embedded in the averaged *Ulysses* data (see, e.g., Laming & Lepri 2007), is likely a reflection of the coronal charge state distribution within streamers similar to the example of streamer 3.

6.3. Connecting Electron Temperatures to Charge States

In situ charge state measurements combined with modeling have been often used to infer the peak electron temperature in the corona, also referred to as the freezing-in temperature (e.g., Owocki et al. 1983; Geiss et al. 1995), and the heliocentric distance associated with this peak. To date, the most comprehensive inferences are those provided by Ko et al. (1997) and Gloeckler & Geiss (2007). Ko et al. (1997) averaged 100 days of SWICS/*Ulysses* data from day of year (DOY) 170 to 270 in 1994 when the Sun was at a minimum of activity during the first south polar pass of the spacecraft. The solar wind speed was almost constant around 780 km s^{-1} when the spacecraft traveled from 69° to 79° south. They inferred a maximum coronal electron temperature of 1.5–1.6 $\times$ 10^6 K over a distance range of 1.3–1.5 $R_\odot$. Using a different approach for the analysis of the *Ulysses* SWICS data, Gloeckler & Geiss (2007) considered the three-year period from late 1993 to 1996 and limited their data selection to wind speeds between 700 and 800 km s^{-1}. By considering charge states of C, N, O, Mg, Si, S, and Fe, they inferred a freezing-in temperature increasing slightly with mass, with an average around 1.1 $\times$ 10^6 K. Their inference for the Fe charge states, in particular, was 1.18 $\times$ 10^6 K.

The range of the Ko et al. (1997) and Gloeckler & Geiss (2007) electron temperature inferences is shown in Figure 6. At first glance, the disparity in their inferences seems to point to uncertainties associated with the different approaches used. However, the Ko et al. (1997) analysis corresponded to a time interval when the average dominant charge state measured by *Ulysses* was Fe^{11+}. The origination of this charge state in the corona would imply emission in Fe XII, which is equivalent to an electron temperature of 1.5–1.6 $\times$ 10^6 K (see Figure 6). The Gloeckler & Geiss (2007) study encompassed a time period dominated by Fe^{10+} even though Fe^{11+} was present in the early part of the three-year period they considered.

Hence, the dominant electron temperature of 10^6 K and the dominant Fe^{10+} charge state in the corona, in the eclipse observations of 2006 and 2008, as described in Sections 6.1 and 6.2, match remarkably well the dominance of Fe^{10+} charge state measured in interplanetary space and the electron freezing-in temperature of 1.18 $\times$ 10^6 K derived from these in situ measurements by Gloeckler & Geiss (2007), albeit from the previous solar minimum. This correspondence establishes an unambiguous link between conditions in the inner corona and interplanetary space.

7. BROADER IMPLICATIONS OF THE ECLIPSE OBSERVATIONS

7.1. Implications of the Observed Ion Density Enhancements

While the spatial distribution of electron temperature in the corona, as shown in Figure 5, has implications for coronal heating processes, so do the localized ion density enhancements first reported in Fe XI emission in the 2006 eclipse observations (Habbal et al. 2007a).

Solar wind models including alpha particles and heavier ions invariably yield localized enhancements in ion densities. Jokipii (1966) was the first to report such an enhancement, which he associated with the peak of the electron temperature in the corona. In other models (e.g., Bürgi & Geiss 1986; Li et al. 1997; Chen et al. 2004; Lie-Svendsen & Esser 2005), the localized enhancements depend on assumed plasma parameters and flow tube geometries. Lie-Svendsen & Esser (2005) interpreted these enhancements as a consequence of a deficit in the energy input to heavy ions which is required for them to remain coupled to the proton flow. Once decoupled, a localized buildup of their density in the corona occurs.

A comparison of the observed localized enhancements in Fe^{10+} ion densities relative to electrons (or equivalently white light) is shown in the lower panels of Figure 2 for the Fe XI emission in 2006 (left) and 2008 (right). The added empirical information provided by further comparison with the temperature maps (Figure 5) is that regions of localized Fe^{10+} enhancements are invariably associated with complex magnetic structures of cool material within streamers and along their boundaries. Hence the complexity of the magnetic field geometry and the temperature of the expanding coronal plasma contribute to localized ion density enhancements. At present, it is not clear what the implications of these density enhancements for the dynamics of the solar wind flow are. On the other hand, the localized enhancements observed in the hotter line of Fe XIV (see Figure 3) are not likely to have anything to do with the solar wind flow at those heights since they appear in the confined plasma within the bulges of streamers.

7.2. Implications for the Thermodynamic Properties of Streamers

The localized ion density enhancements coupled with the electron temperature map of the corona provide insight into a long-standing puzzle regarding the thermodynamic properties of streamers, as first observed with the UVCS on *SOHO* at solar minimum. UVCS measurements on 1996 October 12 (Noci et al. 1997; Raymond et al. 1997), at the absolute minimum of cycle 22, revealed that the bulge of a classical-shaped streamer had reduced O VI emission at 103.19 and 103.76 nm, while this was not the case for Ly α emission. As described in detail in Habbal et al. (2007a), comparison of these ultraviolet observations with the 2006 Fe XI streamer observations (see their Figure 10), although from different solar minima, showed a remarkable resemblance, namely enhanced Fe XI and O VI emission along the boundaries of the streamer relative to its bulge. There was also a marked resemblance between white light and Ly α which showed no distinction between the bulge of the streamers and their boundaries.

The complementary electron temperature information provided by the 2008 eclipse observations is that the bulges of most streamers are comprised of hot (around 2 $\times$ 10^6 K) material (see Figures 3 and 5). At those temperatures, cooler emission lines, such as O VI, cannot be abundant (O VI emission has peak ion formation temperature around 3 $\times$ 10^5 K) since they will be further ionized by collisional excitation with 2 $\times$ 10^6 K electrons. This is not necessarily the case for Ly α emission, since it can be considered a proxy for photons, and hence electrons through charge neutrality, when the plasma is still dominated by collisions (see e.g. Allen et al. 1998). Ly α can be considered a proxy for protons when the plasma is still dominated by collisions (see, e.g., Allen et al. 1998). Consequently, the spatial distribution of the Ly α emission should be similar to the distribution of electrons, i.e., the electron-scattered photospheric emission or white light, in the bulge of streamers as observed.

If that is the case, then observations of reduced O VI emission in the bulges of streamers and enhanced emission along their boundaries should have been reported more frequently by UVCS and should not be limited to solar minimum. There are a few possible explanations for the paucity of such UVCS observations. (1) Unlike eclipse observations, UVCS is not an imager. The UVCS images are reconstructed from spectral measurements made along the slit of the spectrograph as the slit is moved in radial direction and position angle. Comprehensive observations of a given streamer take at least one full day of observations. (2) Streamers do not always appear face-on, such as in the examples of the 2006 northeast streamers, or of the 2008 southeast and southwest streamers labeled 3 and 4 in Figure 4. (3) The bulge of a given streamer has to be extended far enough spatially to appear beyond the inner edge of the UVCS coronagraph, or 1.5 $R_\odot$. Such streamers are more common at solar minimum than at other phases of the solar cycle.

In summary, what the Fe line eclipse observations provide is new insight into the thermodynamics of streamers, namely hot bulges, and cooler boundaries where ion densities can be locally enhanced or trapped. It is plausible that these features contribute to a solar wind from the boundaries of streamers with different characteristics than the wind originating from other open magnetic regions, primarily coronal holes.

8. SUMMARY AND CONCLUSIONS

The eclipse observations in 2006 and 2008 presented here led to the first empirical constraints on the location of the transition from collisional to radiative excitation of a number of Fe spectral lines, a distance referred to as R_t. Knowledge of R_t yielded the first two-dimensional distribution of the electron temperature (below R_t) and of Fe charge states (beyond R_t) in the expanding corona out to a distance of 3 $R_\odot$. R_t varied from 1.1 to 2 $R_\odot$ depending on the Fe charge state and the underlying density structures. R_t was also associated with the distance at which the ion charge states freeze-in, namely, beyond which their ionization state cannot change. The fortuitous availability of in situ measurements from SWICS on *ACE* in 2006 and 2008 in the ecliptic plane, and on *Ulysses* in 2006 at -43° latitude, yielded a very close correspondence between the coronal electron temperature and charge states determined from the eclipse observations with their in situ counterpart. This very close correspondence thus established a direct link between the two.

At the core of these discoveries was the Fe XI line. Its strong radiative relative to collisional excitation was such that the emission could be observed out to several solar radii in the corona. It is precisely this extended emission, within the context of three other Fe spectral lines covering a temperature range of approximately 1–2 $\times 10^6$ K, which provided a comprehensive account of the thermodynamic properties of the inner corona. The limited radial extent of Fe XIII and Fe XIV emission, in comparison with Fe XI, was shown to be an electron temperature bias phenomenon inherent to the corona at the time of these observations at solar minimum.

The resulting electron temperature map showed that the hottest emission in the corona coincides with the bulges of streamers, but that not all streamers have necessarily the same temperature. More importantly, the map showed that the electron temperature of the corona associated with open magnetic structures and the solar wind, whether in polar regions, low latitude coronal holes, or along the boundaries of streamers, is very close to the peak temperature of formation of the Fe XI line, namely in the range of 1–1.2 $\times 10^6$ K during the extended period of low solar activity from 2006 until 2008. This is consistent with earlier inferences of electron temperatures, such as by Habbal et al. (1993) and Wilhelm et al. (1998).

From observations at two eclipses, it has also become clear that localized ion density enhancements do indeed occur in the corona. Such enhancements in low charge states and cool plasmas (i.e., with $T_e \approx 10^6$ K) appear along the boundaries of streamers, at their cusp, and in complex magnetic structures in the distance range of 1.2–1.5 $R_\odot$. Interestingly, the occurrence of ion density enhancements is also inherent to solar wind models which incorporate the behavior of heavy ions. They likely arise as a consequence of the breakdown of collisional coupling between protons and the heavier ions and the subsequent deficit in energy input to the heavier species as proposed by Lie-Svendsen & Esser (2005). As such, the observed enhancements outline the physical location in the corona where this decoupling occurs. On the other hand, localized enhancements in high charge states (e.g., Fe^{13+}) in the bulges of streamers cannot be accounted for by solar wind models since they pertain primarily to closed magnetic structures.

The results presented here underline the uniqueness of eclipse measurements. With exposure times not exceeding 8 s, observations of four Fe spectral lines have enabled us to probe the most critical part of the corona, starting from the solar surface out to a few solar radii, where the solar wind originates and accelerates, and where the coronal plasma undergoes the most rapid changes. At present, no coronagraph can achieve the clarity of these images over this distance range. Imaging of this region in four spectral lines has yielded new insight into the topology of the corona which, if it had been limited to white light, would have missed the most important features. Most importantly, these observations have uncovered novel aspects of the behavior of heavy ions, as well as the electron thermal distribution. They have led to the first empirical determination of the locus, R_t, of the transition from collisionally to radiatively dominated emission for different Fe ions, the two-dimensional distribution in the corona of the electron temperature below that distance and of four Fe charge states beyond.

The eclipse observations of Team 1 were made possible by funding from NASA, grant NNX08AQ29G, NSF grant ATM 08-02520 to the University of Hawaii (S.R.H., J.J., and H.M.), NSF grant ATM-0801633 and a NC Space grant New Investigations award to Appalachian State University (A.D.), and NSF grant NSF-AGS-0450096 to Bridgewater State College (M.A.). Miloslav Druckmüller was supported by grant 205/09/1469 from the Czech Science Foundation. V.R. was partially supported by the Slovak Academy of Sciences Grant Agency VEGA, grant No. 7012, and by the Science and Technology Assistance Agency APVT under contract APVT 51-012-704. M.D. and V.R. also extend their thanks to Peter Aniol, ASTELCO for technical and financial support. We thank Alan Lichty from Princeton Instrument for lending us a PIXIS 1024BR camera for the 2006 eclipse observations. The SWICS Advanced Composition Explorer (ACE) data were provided by the ACE Science Center at http://www.srl.caltech.edu/ACE/ASC/. The SWICS/*Ulysses* data are available at http://helio.esa.int/ulysses/ftp/data/swics/.

REFERENCES

Allen, L. A., Habbal, S. R., & Hu, Y.-Q. 1998, J. Geophys. Res., 103, 6551
Bürgi, A., & Geiss, J. 1986, Sol. Phys., 103, 347

Chen, Y., Esser, R., Strachan, L., & Hu, Y. 2004, ApJ, 602, 415
Druckmüller, M. 2009, ApJ, 706, 1605
Druckmüller, M., Rušin, V., & Minarovjech, M. 2006, Contrib. Astron. Obs. Skalnate Pleso, 36, 131
Esser, R., Edgar, R. J., & Brickhouse, N. S. 1998, ApJ, 498, 448
Gabriel, A. H., et al. 1971, ApJ, 169, 595
Geiss, J., et al. 1995, Sci, 268, 1033
Gloeckler, G., & Geiss, J. 2007, Space Sci. Rev., 130, 139
Gloeckler, G., et al. 1992, A&AS, 92, 267
Gloeckler, G., et al. 1998, Space Sci. Rev., 86, 495
Habbal, S. R., Esser, R., & Arndt, M. B. 1993, ApJ, 413, 435
Habbal, S. R., Morgan, H., Johnson, J., Arndt, M. B., Daw, A., Jaeggli, S., Kuhn, J., & Mickey, D. 2007a, ApJ, 663, 598
Habbal, S. R., Morgan, H., Johnson, J., Arndt, M. B., Daw, A., Jaeggli, S., Kuhn, J., & Mickey, D. 2007b, ApJ, 670, 1521
Hundhausen, A. 1968, Space Sci. Rev., 8, 690
Jokipii, J. R. 1966, in The Solar Wind, ed. R. J. Mackin, Jr. & M. Neugebauer (Oxford: Permanon Press), 215
Judge, P. G. 1998, ApJ, 500, 1009
Ko, Y.-K., Fisk, L. A., Geiss, J., Gloeckler, G., & Guhathakurta, M. 1997, Sol. Phys., 171, 345
Kohl, J. L., Noci, G., Cranmer, S. R., & Raymond, J. C. 2006, A&AR, 13, 31
Kohl, J. L., et al. 1995, Sol. Phys., 162, 313
Laming, J. M., & Lepri, S. T. 2007, ApJ, 660, 1642
Li, X., Esser, R., Habbal, S. R., & Hu, Y.-Q. 1997, J. Geophys. Res., 102, 17419
Li, X., Habbal, S. R., Kohl, J., & Noci, G. 1998, ApJ, 501, L133
Lie-Svendsen, Ø., & Esser, R. 2005, ApJ, 618, 1057
Mazzotta, P., Mazzitelli, G., Colafrancesco, S., & Vittorio, N. 1998, A&AS, 133, 403
Morgan, H., & Habbal, S. R. 2007, A&A, 465, L47
Morgan, H., Habbal, S. R., & Woo, R. 2006, Sol. Phys., 236, 263
Noci, G., et al. 1997, Adv. Space Res., 20, 2219
Owocki, S. P., Holzer, T. E., & Hundhausen, A. J. 1983, ApJ, 275, 354
Pasachoff, J. M., Rusin, V., Druckmuller, M., Aniol, P., Saniga, M., & Minarovjech, M. 2009, ApJ, 702, 1297
Raymond, J. C., et al. 1997, Sol. Phys., 175, 645
Wilhelm, K., et al. 1998, ApJ, 500, 1023